The International Journal of Advanced Manufacturing Technology
https://doi.org/10.1007/s00170-026-17732-3

ORIGINAL ARTICLE

Machine learning-based prediction of thermal profiles during laser-based additive manufacturing

Aishwarya Manjunath[1,2] · **Venkata Mani Krishna Karri**[1] · **Amrutha Anantatamukala**[1] · **Selvamurugan Palaniappan**[1,3] · **Shashank Sharma**[1,3] · **Song Fu**[2] · **Narendra B. Dahotre**[1,3]

Received: 26 December 2025 / Accepted: 11 February 2026

Abstract

Laser Powder Bed Fusion (L-PBF) is distinguished by its precision in fabricating intricate structures, yet accurately predicting thermal profiles remains challenging due to the computational complexity of traditional physics-based models. This study explores the application of the Pix2Pix Generative Adversarial Network (GAN) framework for predicting thermal maps in L-PBF processes across multiple materials, including 316 stainless steel alloy (SS316L), aluminum alloy (AlSi10Mg), pure copper (Cu), and pure tungsten (W). Unlike conventional image-to-image translation tasks, where input and output images exhibit pixel-to-pixel spatial correlation, this work maps additive manufacturing process parameters encoded as images lacking spatial correlation to thermal profiles representing temperature distributions. The proposed approach demonstrates high accuracy (Mean Squared Error (MSE) $< \mathbf{0.018}\%$ and Structural Similarity Index Measure (SSIM) $> \mathbf{92.5}\%$) and rapid prediction speeds (100 images per second) using data derived from finite element simulations, which were validated with experimental results. This study provides a computationally efficient methodology for thermal profile prediction, showcasing the utility of GANs in capturing the relationship between process parameters and thermal behavior in additive manufacturing.

Keywords Machine learning · Thermal profiles · Additive manufacturing · Finite element method · Deep learning · Generative adversarial networks

✉ Narendra B. Dahotre
narendra.dahotre@unt.edu

Aishwarya Manjunath
aishwaryamanjunath@my.unt.edu

Venkata Mani Krishna Karri
venkatamanikrishna.karri@unt.edu

Amrutha Anantatamukala
amrutha.anantatamukala@unt.edu

Selvamurugan Palaniappan
SelvamuruganP@my.unt.edu

Shashank Sharma
shashank.sharma@unt.edu

Song Fu
song.fu@unt.edu

[1] Center for Agile and Adaptive Additive Manufacturing (CAAAM), University of North Texas, Denton, TX 76207, USA

[2] Department of Computer Science, University of North Texas, Denton, TX 76207, USA

[3] Department of Material Science and Engineering, University of North Texas, Denton, TX 76207, USA

1 List of symbols

Symbol	Description	**Units**
ρ	Density	$\mathrm{kg/m^3}$
C_p	Specific heat	J/(kg K)
k	Thermal conductivity	W/(m K)
q'''	Volumetric heat source	$\mathrm{W/m^3}$
T	Temperature	K
ϵ	Emissivity of irradiated surface	-
σ_b	Stefan-Boltzmann coefficient	$\mathrm{W/(m^2 \cdot K^4)}$
n	Normal unit vector direction	-
q_{evap}	Vaporization heat flux	$\mathrm{W/m^2}$
M_v	Mass loss due to vaporization	kg
L_v	Latent heat of vaporization	$\mathrm{J/kg}$
k_b	Boltzmann constant	$\mathrm{J/K}$
T_s	Surface temperature	K
P_{amb}	Ambient pressure	Pa
ΔH_v	Enthalpy of vaporization	J/(kg K)
T_v	Vaporization temperature	K
g	Heat source scaling constant	-
r_b	Laser beam radius	mm
H	Melt pool depth scaling constant	mm
P	Laser power	W
α_{th}	Thermal diffusivity	$\mathrm{m^2/s}$
τ	Laser interaction time	s
V	Scanning speed	$\mathrm{m/s}$
A, n	Material fitting constants	-

2 Introduction

Additive manufacturing (AM) has emerged as a transformative manufacturing paradigm for producing geometrically complex components with reduced material waste and shortened production cycles compared to conventional subtractive methods [1]. Among metal AM technologies, Laser Powder Bed Fusion (L-PBF) is particularly attractive due to its capability to fabricate high-density components with fine geometric resolution and consistent quality [2]. In L-PBF, a focused laser selectively melts metallic powder in a layerwise manner, resulting in highly localized and transient thermal gradients governed by laser–material interaction, heat transfer, melting and solidification, and phase transformation phenomena [3].

The spatiotemporal thermal profile produced during L-PBF plays a central role in determining melt pool geometry, solidification dynamics, residual stress evolution, and ultimately microstructure and mechanical properties [4]. Consequently, accurate prediction of thermal fields is a prerequisite for process optimization, defect mitigation, and digital twin development. Recent studies on additively manufactured NiTi alloys for elastocaloric refrigeration further highlight the strong coupling between process-induced thermal history, microstructural evolution, and functional performance, underscoring the importance of accurate thermal control and prediction in laser-based AM processes [5–8]. Physics-based numerical frameworks such as finite element methods (FEM), computational fluid dynamics (CFD), and lattice Boltzmann methods (LBM) have been extensively used to model thermal behavior in AM processes [9, 10]. While these models provide physically interpretable results, their high computational cost limits their applicability for real-time prediction, parametric sensitivity analysis, and large-scale process optimization [11].

To overcome these limitations, data-driven machine learning (ML) models have been explored as computationally efficient surrogates for thermal prediction. Early efforts employed tree-based models and convolutional neural networks (CNNs) to predict temperature evolution and melt pool characteristics in laser-based AM processes [3, 12]. Although these approaches demonstrated reduced inference time, they often required large training datasets, exhibited limited generalization across materials, or struggled to capture sharp thermal gradients intrinsic to L-PBF. More recent studies combined neural networks with reduced-order physics representations or hybrid architectures to improve accuracy; however, adapting such models to new materials or process windows typically required retraining or redesign, limiting scalability.

Physics-informed machine learning (PIML) approaches were subsequently proposed to embed governing equations or physical constraints directly into neural networks [13]. Models such as physics informed neural networks (PINNs) and recurrent neural network (RNN)-based frameworks have shown promise in predicting three-dimensional thermal fields while reducing dependence on large labeled datasets [9, 14]. Despite these advantages, incorporating complex thermo-physical mechanisms into the learning process remains computationally demanding, and model training becomes increasingly challenging as dimensionality and material diversity increase.

Generative Adversarial Networks (GANs) offer an alternative paradigm for learning high-dimensional thermal fields by directly modeling the distribution of temperature maps rather than regressing individual scalar quantities. GANs have been successfully applied across image synthesis, scientific simulation, and materials informatics, where they have demonstrated superior capability in capturing complex spatial patterns and sharp discontinuities [15, 16]. In the context of additive manufacturing, GAN-based models have been used to generate microstructures, predict material morphology, and synthesize thermal or process-related images [17, 18]. However, conventional GANs lack explicit mechanisms to generate outputs conditioned on prescribed process parameters, limiting their utility for process-aware thermal prediction.

Conditional GANs (CGANs) address this limitation by learning mappings between conditioned inputs and target outputs [19]. Several recent studies have applied CGAN variants to thermal modeling problems by conditioning on discrete process labels, layer indices, or spatially aligned input images [20, 21]. These approaches are effective when conditioning variables are categorical or when input images share pixel-wise spatial correspondence with the target thermal fields. However, L-PBF process parameters such as laser power, scan speed, and time are continuous and non-spatial by nature, posing a fundamental challenge for image-to-image translation frameworks that typically rely on spatial alignment. Representative prior studies and their key characteristics, including their key limitations, are summarized in Table 1.

Building on the limitations summarized in Table 1, the present work demonstrates that a conditional Pix2Pix GAN can reconstruct high-fidelity thermal profiles directly from non-spatial process-parameter encodings, without requiring pixel-wise correspondence between input and output images. By encoding continuous laser power, scan speed, and temporal information into structured, non-spatial representations, the model learns the underlying physical mapping between process parameters and spatial temperature fields, rather than relying on spatially correlated inputs, prior thermal images, or discrete labels as used in existing GAN-based thermal models. This conditioning strategy enables learning across continuous process-parameter spaces and improves generalization across materials. The approach is validated across four materials—SS316L, AlSi10Mg, Cu, and W—spanning a wide range of thermophysical properties, thereby emphasizing generality rather than material-specific tuning. By leveraging FEM-generated thermal data whose melt pool geometries and aspect ratios are experimentally calibrated, the proposed GAN framework is intended as a high-fidelity surrogate of the underlying FEM model. As such, the predictive accuracy of the proposed approach is inherently bounded by the fidelity of the numerical simulations used for training, rather than constituting a direct experimental predictor. The key contribution of this work lies not in introducing a new GAN architecture, but in demonstrating that an existing, well-established Pix2Pix framework can be repurposed in an architecture-agnostic manner to learn physically meaningful thermal fields from non-spatial process-parameter encodings. This insight expands the applicability of image-to-image GANs for thermal modeling in L-PBF and supports their use in rapid process exploration, sensitivity analysis, and digital twin applications. Since numerous variants of the Pix2Pix and conditional GAN architectures have been reported in the literature [22], the proposed strategy offers a practical

Table 1 Summary of related work on machine learning–based thermal profile prediction in laser-based additive manufacturing

Reference	Model Type	Conditioning / Inputs	Material Scope	Key Limitations
Ness et al. [3]	Tree-based ensemble ML	Process parameters and voxel-wise thermal history	Single (L-PBF, IN718)	High data requirements; computationally expensive training; limited scalability to new materials
Hemmasian et al. [12]	CNN	Laser power, scan speed, and time	Single (L-PBF, Ti-6Al-4VF)	Difficulty capturing sharp thermal gradients; limited generalization
Xu et al. [23]	MLP + CNN	Beam parameters	Single (L-PBF metal alloy)	Predicts representative melt-pool profiles rather than full transient history; trained for one alloy and machine setup
Ren et al. [14]	Physics-informed ML (RNN)	FEM-informed scan history and thermal data	Single (LAAM, H13 tool steel)	Requires model reconstruction for new materials and increased training complexity
Xie et al. [9]	Physics-informed neural network (PINN)	Governing heat transfer equations with sparse data	Single (DED, metal alloy)	Computationally intensive training; limited scalability to high-dimensional datasets
Ouidadi et al. [20]	MPS-GAN	Discrete process-parameter labels	Per-dataset single process/material (spot welding; AM)	Trained only on a discrete set of build-parameter combinations and specific material–process datasets; generalization to unseen process conditions or new materials is not established
Zhou et al. [21]	LMD-cGAN	Layer index and prior thermal images	Single (LMD, Ti-6Al-4V)	Relies on spatially correlated in-situ thermal images; does not condition explicitly on continuous process parameters

and extensible advantage. By designing the input pipeline to conform to the canonical Pix2Pix conditioning interface, diverse state-of-the-art Pix2Pix-based architectures can be directly adopted without modifying the core network design. This decoupling of input representation from architectural choices enables researchers to readily experiment with and benchmark multiple advanced Pix2Pix variants by simply adapting the process-parameter encoding, rather than re-engineering the model itself. As a result, the present approach significantly lowers the barrier to entry, promotes architectural interoperability, and makes recent advances in conditional GANs readily accessible to a broader materials and manufacturing research community.

3 Dataset

3.1 Data generation

3.1.1 Numerical model

The present study employed a 3D FEM-based heat transfer model to generate multi-track thermal profiles during L-PBF-based AM. As reported in the literature, laser-matter interaction involves complex phenomena such as multiple reflections of the laser beam, highly dynamic melt pool convection, and vaporization-induced melt pool oscillations [24]. The dynamic coupling of laser absorption and melt pool oscillation results in different modes of melting (conduction, transition, and keyhole) with variations in process parameters (laser power, scanning velocity, hatch spacing, and layer thickness) [25, 26]. In light of these considerations, incorporating the aforementioned physical aspects into the numerical model is essential for accurately representing thermal profiles in the L-PBF process. However, the inclusion of such complex phenomena inevitably leads to increased computational run-time, which can hinder the generation of the extensive datasets required for ML algorithms [24, 25, 27]. Therefore, to efficiently generate a sufficient dataset for a GAN-based deep learning framework, a computationally tractable approach was adopted. In this approach, the laser-matter interaction and melt pool convection were compensated by an experimentally derived volumetric heat source [28, 29]. Primarily, as a proof of concept, thermal profiles for up to five tracks on a single layer were generated and utilized as the input dataset for the GAN-based machine learning framework. It is important to note that this framework is not limited to single-layer predictions; the numerical model and the resulting machine learning predictions can be seamlessly extended to accommodate multi-track, multi-layer thermal profile predictions. Parametric variations in machine settings and changes in material properties were employed to produce a diverse set of thermal profile data. The mathematical formulation and the modeling framework are described in the following subsections.

3.1.2 3D transient thermal model

The governing equation related to the heat transfer model is expressed as the following equation [24, 25]:

$$\rho C_p \frac{\partial T}{\partial t} = \nabla \cdot (k \nabla T) + q''' \tag{1}$$

In the above equation, the delineation between the powder bed and the melt pool was employed using the effective thermal properties of the powder bed, accounting for the inter-particle porosity. The effective density of the powder bed (ρ_p) can be expressed as [30].

$$\rho_p = \begin{cases} (1-\phi)\rho, & T < T_m \\ \rho, & T > T_m \end{cases} \tag{2}$$

A similar expression can be used for specific heat C_p. The effective thermal conductivity (k_p) of the powder bed was modeled as a function of the bulk thermal conductivity (k), the thermal conductivity of the surrounding gas or air (k_a), the powder packing density (ϕ), and the radiative effects within the powder bed (k_r). This relationship is captured in the following Eq. 3 [31]:

$$\frac{k_p}{k_a} = \left(1 - \sqrt{1-\phi}\right)\left(1 + \phi \frac{k_r}{k_a}\right) + \sqrt{1-\phi}\left[\frac{2}{1 - \frac{k_a}{k}}\left(\frac{k}{k_a} \ln\left(\frac{k}{k_a}\right) - 1\right) + \frac{k_r}{k_a}\right] \tag{3}$$

The laser-irradiated surface of the computational domain was prescribed with the following conditions:

$$-k \frac{\partial T}{\partial z} = -h_c \left[T - T_{\text{amb}}\right] - \epsilon \sigma_b \left[T^4 - T_{\text{amb}}^4\right] \tag{4}$$

The non-irradiated boundary surfaces were prescribed with the following boundary condition:

$$-k \frac{\partial T}{\partial n} = -h_c \left[T - T_{\text{amb}}\right] \tag{5}$$

The vaporization heat flux, which accounts for heat loss due to material vaporization, can be expressed as:

$$q_{\text{evap}} = M_v \times L_v \tag{6}$$

where the mass loss due to vaporization can be expressed as:

$$M_v = m\sqrt{\frac{2\pi k_b T_s}{m}} \times P_{\text{amb}} \times \exp\left(\frac{\Delta H_v}{k_b T_v}\left(1-\frac{T_v}{T_s}\right)\right) \tag{7}$$

3.1.3 Volumetric heat source

As outlined in the preceding sections, the thermal model adopted in this study neglected certain physical mechanisms, including melt pool convection and the interaction of laser energy with the powder bed, such as multiple internal reflections, which are likely to influence the evolution of melt pool morphology during L-PBF. To address this, a volumetric heat source was scaled using the experimentally observed melt pool depth. In the L-PBF process, the melt pool depth varies with changes in material properties and machine parameters. According to the literature, a normalized energy input-based analytical function can be constructed to obtain a scaling function for the experimentally measured melt pool depth [32–36]. This scaling function is formulated to include phenomenological factors such as laser intensity, laser absorption coefficient, laser interaction time, thermal diffusivity, specific heat, and melting temperature. Consequently, this volumetric heat formulation enables a reasonable approximation of the changes in melting mode and thermal profiles that occur with varying machine parameters and material properties. The following formulation describes the volumetric heat source [37]:

$$q''' = \frac{g\alpha P}{\pi r_b^2(z)} \exp\left(-\frac{gr^2}{r_b^2(z)}\right) f(z); \quad f(z) = \frac{1}{H}\exp\left(-\frac{g|z|}{H}\right) \tag{8}$$

In the above formulation, the term H corresponds to the melt pool depth, which is scaled using the following normalized energy input-based analytical equation [32, 35]:

$$H = r_b \times A \times \left[\left(\frac{\alpha P}{\pi r_b^2}\right) \times \left(\frac{\tau}{\sqrt{\alpha_{th}\tau}}\right) \times \left(\frac{1}{\rho C_p T_s}\right)\right]^n, \quad \text{where } \tau = \frac{r_b}{V} \tag{9}$$

The parameters A and n are material fitting constants, which can be obtained by fitting the above equation with experimentally obtained melt pool depth values. Thus, the above set of equations completes the conduction-based heat transfer formulation of the L-PBF process. In this study, four different material systems were considered: SS316L, W, Cu, and AlSi10Mg. These materials were selected due to their significant variation in thermophysical properties, such as thermal conductivity and melting point. Note that α is the laser absorption coefficient. In the current framework, at any given point below the melting temperature, α has been assigned a value pertaining to powder bed absorption. In case the temperature exceeds the melting temperature, α has been assigned the value of the molten metal absorption coefficient. The values for powder bed and molten metal absorption coefficients were obtained from the literature for the respective material systems: SS316L [34], W [37, 38], Cu [39], and AlSi10Mg [32]. The machine parameters and the values of the thermophysical properties used to evaluate (1)–(9) are listed in Tables 2 and 3, respectively. The number of data files per material listed in Table 2 depends on the power and velocity parameters for that particular

Table 2 List of process parameters employed in input dataset generation

Parameter	W	SS316L	Cu	AlSi10Mg
Laser Power (W)	400–900	100–250	250–500	100–250
Scanning Speed (m/s)	0.1–0.5	0.3–1.5	0.3–1.0	0.3–1.5
Hatch Spacing (mm)	0.05	0.05	0.05	0.05
Beam Radius (mm)	0.04	0.0275	0.0275	0.0275
Layer Thickness (mm)	0.03	0.05	0.05	0.05
Beam Adjustment Factor (g)	2.0	2.0	2.0	2.0
Time Steps (s)	1×10^{-4}	1×10^{-4}	1×10^{-4}	1×10^{-4}
Total Number of Data Files	13013	4459	3558	5544

Table 3 Thermophysical parameters employed in the 3D heat transfer model. References for data sources are provided

Thermophysical Property	W [37, 40]	SS316L [40, 41]	Cu [40, 42, 43]	AlSi10Mg [30, 40, 44]
Density, Solid (kg/m^3)	19300	7950	8960	2670
Density, Liquid (kg/m^3)	16826	$8200 - 0.77T$	8020	2670
Conductivity, Solid (W/(m K))	180	$9.23 + 0.0139T$	385	$247.63 - 0.042T$
Conductivity, Liquid (W/(m K))	97	$5.5 + 0.0133T$	157	$72.07 + 0.020T$
Specific Heat, Solid (J/(kg K))	131	$415 + 0.01838T$	481	$834.96 + 0.216T$
Specific Heat, Liquid (J/(kg K))	274	830	537	1050
Heat of Melting (kJ/mol)	35.3	15.5	13.1	10.8
Heat of Vaporization (kJ/mol)	800	380	300	293 (Aluminum)
Liquidus Temperature (K)	3695 (melting)	1723	1357 (melting)	867
Solidus Temperature (K)	-	1658	-	831
Vaporization Temperature (K)	5555	3090	2835	2743
Boltzmann Constant (J/K)	1.328×10^{-23}	1.328×10^{-23}	1.328×10^{-23}	1.328×10^{-23}
Convective Heat Transfer Coefficient (W/(m^2·K))	15	15	15	15
A, n	0.43, 1.19	0.14, 1.47	0.17, 1.18	0.18, 1.19

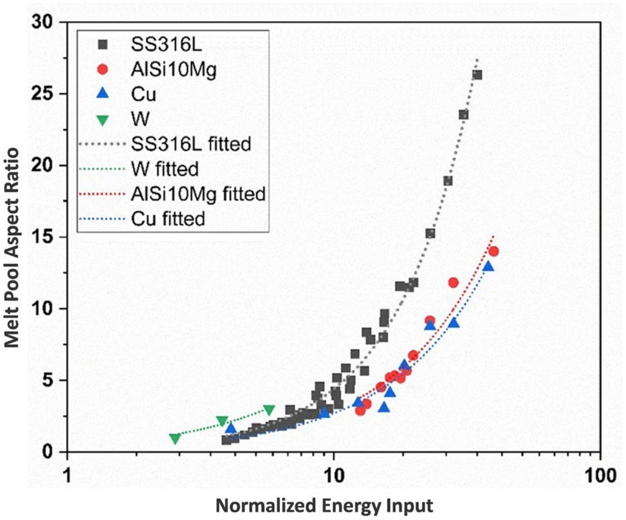

Fig. 1 Melt pool aspect ratio (H/r_b) as function of normalized energy input $\left(\alpha P\pi r_b^2 \times \sqrt{\frac{\tau_{\alpha th}}{\tau}} \times \frac{1}{\rho C_p T_s}\right)$ for different material systems [30, 37, 40–44]

material. Additionally, Eq. 9 was fitted using melt pool depth data for the respective material systems obtained from both literature and in-house experiments. The fitted dataset is plotted in Fig. 1 for reference, and the fitting constants are provided in Table 3 [30, 37, 40–44].

The developed numerical framework was implemented within the commercial FEM software COMSOL Multiphysics®. To resolve the multitrack heating of the laser beam, an adaptive meshing strategy with quadrilateral mapped elements was employed. The minimum mesh size, determined through convergence analysis, ranged from 2 to 15 μm depending on the given process parameter set. The computations were performed on an Intel® Xeon® Gold 6252 CPU (2.10 GHz, 190 GB RAM) processor. Figure 2 presents the transverse cross-sections of numerically simulated melt pool geometries alongside the experimental results for all four material systems. The melt pool dimensions obtained from the numerical model, using the aforementioned analytical functions, are in strong agreement with the experimental data. Furthermore, the melt pool aspect ratio (depth-to-half-width ratio) predicted by the developed numerical model shows good correlation with the experimentally measured values (Fig. 3). Within the current framework, the choice of experimental validation using the melt pool aspect ratio was based on the distinct melting modes observed in laser powder bed fusion. As reported in the literature, three melting modes exist during laser powder bed interaction: conduction, transition, and keyhole modes [24]. These melting modes are contingent on process parameters and dictate the coupling between the laser beam and the molten pool, which significantly influences the melt pool geometry and the evolved temperature within the molten zone.

Given that the present framework considers the laser-matter interaction as a pure conduction problem with

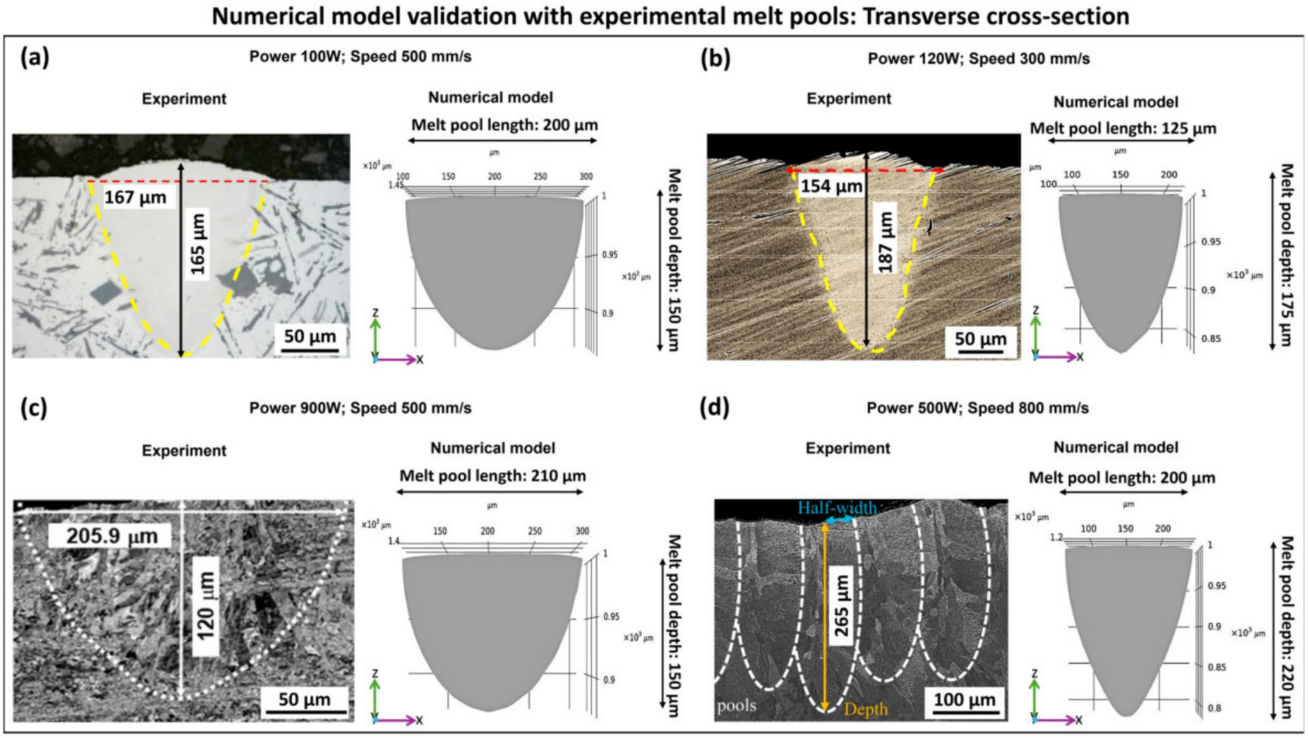

Fig. 2 Comparison of numerically simulated melt pool geometries with experimental results for (**a**) AlSi10Mg [45] (**b**) SS316L (**c**) W [37] (**d**) Cu [39] alloys

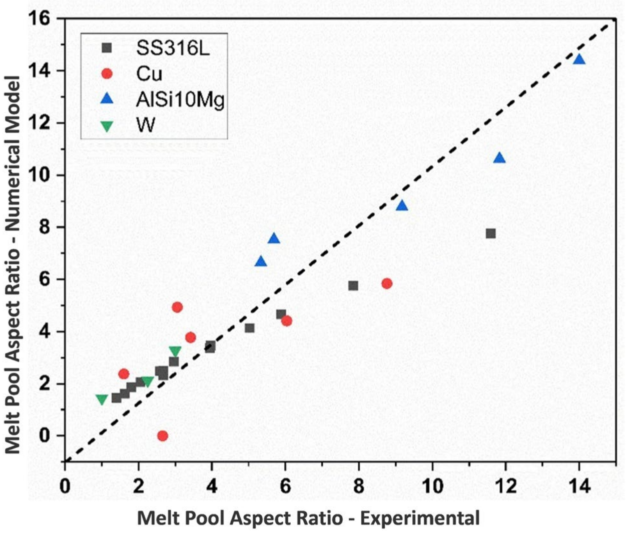

Fig. 3 Comparison of experimentally observed and numerical model based prediction of melt pool aspect ratios (H/r_b)

appropriate vaporization heat source and sink terms, an accurate estimation of the molten volume is essential to establish a reasonable representation of thermal evolution. Moreover, as suggested in the literature, the small diameter of the laser beam and the low laser interaction time ($\leq 1\,\mathrm{ms}$) pose challenges for experimental measurements of thermal evolution within the laser-matter interaction zone in L-PBF [24, 25].

In this context, the present framework, within its current limitations, provides reasonable validation in terms of the melt pool aspect ratio, effectively reflecting the prevailing melting mode, and the corresponding thermal evolution.

3.1.4 Experimental method

In the present framework, the melt pool aspect ratio for the material systems SS316L and tungsten (W) was evaluated through in-house experiments. For SS316L, single-track L-PBF experiments were conducted using a Trumpf TruPrint 1000 machine with a laser beam diameter of 55 $\mu\mathrm{m}$. The SS316L powders, procured from ThermoFisher®, had a D_{50} particle size of 35 $\mu\mathrm{m}$. For tungsten, single-track experiments were performed using an Aconity MDI L-PBF machine with a laser beam diameter of 80 $\mu\mathrm{m}$. Spherical tungsten powder with 99.9% purity and a mean particle size of 33 $\mu\mathrm{m}$ was used. The process parameters for both material systems are listed in Table 2.

Post-processing, the single-track specimens were cross-sectioned, polished, and subjected to metallographic analysis to determine the melt pool morphology (for aspect ratio calculation) using a Keyence VKS laser profilometer. Additional data on the material systems utilized in the modeling framework were obtained from the literature.

3.2 Data pre-processing

The thermal profiles acquired from FEM simulations of four materials SS316L, AlSi10Mg, Cu, and W across different power and velocity combinations from Table 4, were used to test the proposed approach on a broader dataset that reflects realistic additive manufacturing conditions. Table 2 shows the total number of data files created for this work. The CGANs model, being an image translation model, required both source and target data to be in image form.

For this, the numerical data of process parameters laser power, velocity, and time step were encoded into images. For each of the FEM output temperature distribution maps (ground truth), corresponding laser power (P), velocity (V), and time step (t) values were converted into three grids of equal areas in a 256x256 image corresponding to each process parameter, as presented in Fig. 4. In order to maintain consistency and improve model performance, normalization was implemented for power, velocity, and time step. Normalization is crucial in this context as it ensures that all process parameters are on a comparable scale, preventing any one parameter from disproportionately influencing the model. This helps the model to learn more effectively, as it can focus on the relationships between the parameters rather than being biased by differences in their magnitudes, ultimately improving its ability to predict accurate thermal profiles. For the output or ground truth images representing temperature profile maps, logarithmic scaling of temperature values was employed instead of using absolute values. This decision was guided by the observation that logarithmic preprocessing significantly enhanced model convergence during training. The thermal profiles generated by FEM simulations often exhibit a broad range of temperature values, with some regions experiencing extreme localized high values (i.e., near the laser beam) while others remain comparatively low. Such disparities can pose challenges for the model, leading to slower or less effective learning. Logarithmic scaling effectively compresses this wide range, emphasizing smaller but crucial variations in temperature, thereby enabling the model to learn more efficiently and achieve higher accuracy in predicting thermal

Table 4 Laser power and velocity values for each material

Material	Power (W)	Velocity (m/s)
SS316L	100, 125, 150, 175, 200, 225, 250	0.3, 0.5, 0.7, 0.9, 1.1, 1.3, 1.5
AlSi10Mg	100, 125, 150, 175, 200, 225, 250	0.3, 0.5, 0.7, 0.9, 1.1, 1.3, 1.5
Cu	250, 300, 350, 400, 450, 500	0.3, 0.5, 0.75, 1.1
W	400, 450, 500, 550, 600, 650, 700, 750, 800, 850, 900	0.1, 0.3, 0.5

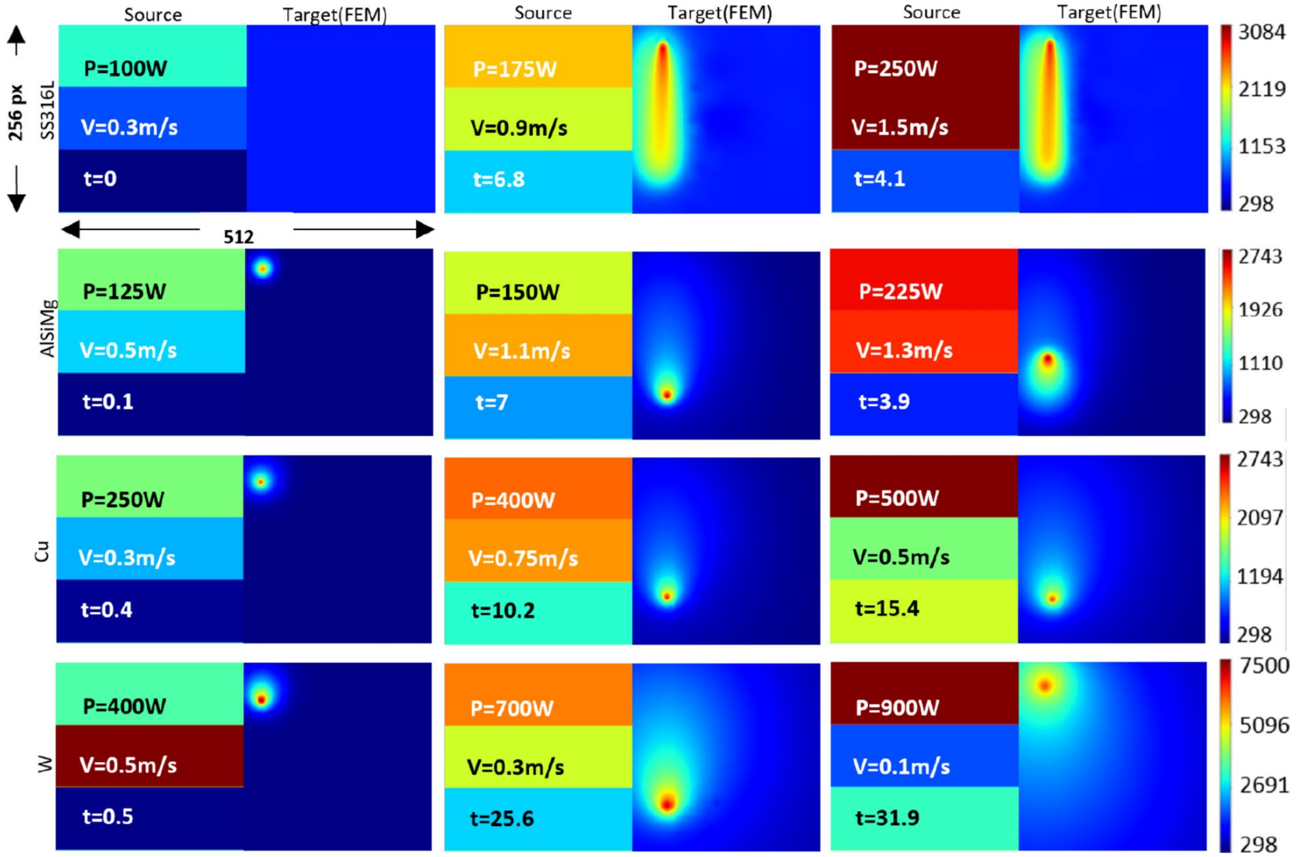

Fig. 4 Source (codified process parameter image) and FEM-generated target images (thermal profiles) for materials SS316L, AlSi10Mg, Cu, and W. Each 256x512 composite image combines a 256x256 source image (left - excluding the labels) and a corresponding 256x256 FEM-generated target image (right), illustrating the differences for the specified materials and process parameters

Table 5 Details of the normalization values for source and target images across all materials

Material	Power (W)	Velocity (m/s)	Time Step	Lowest Temperature (K)	Highest Temperature (K)
SS316L	250	1.5	20.6	188	3084
AlSi10Mg	250	1.5	25.6	293	2743
Cu	500	1	25.6	291	3000
W	900	0.5	77	287	7500

profiles. Thus, the target image of dimensions 256x256 represents a contour plot of thermal profiles from the numerical data derived from the FEM simulation with respect to x and y coordinates. Furthermore, the target image was processed by applying logarithms and normalizing the data with the lowest and highest temperatures for each material, as per the values presented in Table 5.

The processed source and target images were stitched together to create a single 256x512 image (training example), as depicted in Fig. 4. These composite images were then divided into training and testing datasets. The SS316L dataset consists of 3,978 training images and 481 testing images. Among the testing images, 57 were organized into a time series corresponding to a specific combination of power and velocity, while the remaining images were randomly sampled from the dataset. The AlSi10Mg dataset comprises 4,946 training images and 598 testing images, with 71 images structured in a time series. The Cu dataset includes 3,084 training images and 474 testing images, of which 155 images were organized in a time series. Finally, the W dataset contains 11,532 training images and 1,481 testing images, with 257 images arranged in a time series. This non-spatial encoding of continuous process parameters into 256×256 images for image-to-image translation differs from MPS-GAN , which conditions on discrete labels (e.g., sheet number, coating status, welding current), and LMD-cGAN , which uses prior thermal images and layer index [20, 21]. The proposed strategy enables learning thermal responses across continuous power–velocity–time variations for multiple alloys, supporting parametric sensitivity analysis in L-PBF.

4 Methodology

4.1 Network architecture

The CGAN-based machine learning model employs the Pix-2Pix architecture to predict thermal profiles, demonstrating the adaptability of the image-to-image translation approach in GAN-based deep learning without modification. Generative Adversarial Networks (GANs) have been recognized as a pioneering approach to generative modeling in deep learning, frequently utilizing Convolutional Neural Networks (CNNs) [46]. GANs have been employed for various tasks, including image translation [47] and segmentation [48, 49], by framing the problem as a supervised learning task involving two sub-models: the The "Generator model (G)" and the "Discriminator model (D)". These models are trained simultaneously in an adversarial, zero-sum game setting, where the generator aims to deceive the discriminator until the latter becomes uncertain about the classification of the images approximately half of the time [49].

The Generative Adversarial Network (GAN) framework operates in two distinct phases: training and inference. During the training phase, the generator is conditioned on source images that include process parameters such as laser power (P), velocity (V), and time step (t), while also receiving target images that represent the ground truth thermal profiles derived from FEM simulations. Initially, the generator's output is far from the target, allowing the discriminator to effectively distinguish between real and generated images. Through backpropagation and iterative optimization, the generator adjusts its weights to minimize the error between the generated and real images, leading to progressively more accurate thermal profile predictions over time [50–52]. During inference, only the source images are provided to the generator, which then produces the thermal profiles based on these inputs, without the need for target images. This enables the model to generate accurate predictions in the absence of ground truth data.

In artificial neural networks, model weights controlled the flow of information between neurons, determining how data was transformed as it traversed the network [52]. During training, these weights were optimized to minimize prediction errors, enabling the network to learn from the data [52]. The objective was to find optimal weights that minimized the discrepancy between generated and ground truth images [52]. Model weights were typically updated after each batch of training examples, with training progress monitored by evaluating the generator's loss value at regular intervals (epochs) [52].

During the inference phase, the model was tested on unseen data to estimate accuracy using metrics such as mean squared error (MSE) and structural similarity index (SSIM) [53]. After training, the learned model weights were applied for inference on new data, for predicting thermal profiles [54]. In this phase, only the generator network was utilized, while the discriminator network was no longer involved [54].

The success of training GANs depends on several factors, including network architecture, activation functions, loss functions, relative loss weights, and optimization algorithms [52]. In this study, the generator was based on the U-Net architecture within the Pix2Pix framework. It processed the stitched source and target images as input, as illustrated in Fig. 5. The U-Net architecture consisted of encoder and decoder stages with skip connections to enhance feature representation and flow of higher-level information/features to lower levels (due to skip connections) [55]. The network employed standard Convolution - Batch Normalization - ReLU blocks, using 4×4 spatial filters with a stride of 2. The Adam optimizer was chosen for training the GANs due to its fast convergence and adaptive learning rates based on past gradients [51]

The loss functions of the generator:

$$G^* = \arg\min_G \max_D \mathcal{L}_{CGANs}(G, D) + \lambda_{L1}\mathcal{L}_{L1}(G) + \lambda_{L2}\mathcal{L}_{L2}(G) \tag{10}$$

Where, $\mathcal{L}_{L1}(G)$, $\mathcal{L}_{L2}(G)$, and $\mathcal{L}_{CGANs}(G, D)$ represents the L1, L2, and CGANs losses of the generator, respectively. λ_{L1} and λ_{L2} denotes the weights for the L1 and L2 losses respectively. The losses $\mathcal{L}_{L1}(G)$, $\mathcal{L}_{L2}(G)$, and $\mathcal{L}_{CGANs}(G, D)$ are defined as follows:

$$\mathcal{L}_{CGANs}(G, D) = \mathbb{E}_y[\log D(y)] + \mathbb{E}_{x,z}[\log(1 - D(G(x, z)))] \tag{11}$$

$$\mathcal{L}_{L1}(G) = \frac{1}{N}\sum |G(x, z) - y| \tag{12}$$

$$\mathcal{L}_{L2}(G) = \frac{1}{N}\sum (G(x, z) - y)^2 \tag{13}$$

L1 and L2 losses measure the differences between predicted and actual images, crucial in GAN training. $\mathcal{L}_{CGANs}$ corresponds to the binary cross-entropy loss, which typically exhibits high values with correct identification of the real image and low values when the discriminator cannot distinguish real from generated images.

This loss guides the generator's improvement. x and y are source and ground truth images, respectively, while $G(x, z)$ denoted the generator's output. The parameters λ_{L1} and λ_{L2} were used to balance the L1 and L2 losses in the generator's total loss G. Achieving the correct balance between these losses was crucial for optimizing the generator's output, ensuring that the generated images closely resembled the ground truth images.

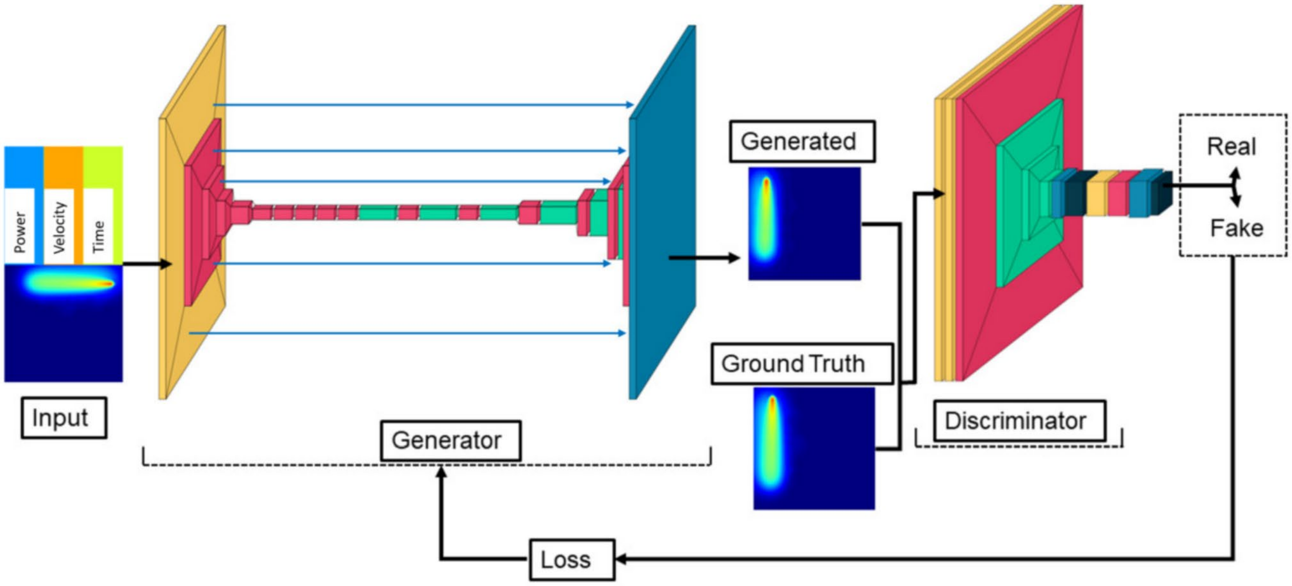

Fig. 5 Illustration of CGANs machine learning model architecture used for predicting thermal profiles

Although the adversarial loss functions in Eqs. 10–13 were expressed in a compact form, the proposed framework was conditional in an architectural sense. Within the present Pix2Pix implementation, thermal profiles were not provided to the discriminator in isolation. Instead, paired inputs comprising a codified process–parameter image and the corresponding real or generated thermal profile were supplied. The conditioning variables (actual experimental process parameters), such as laser power, scan velocity, and time step, were embedded directly within the input image as graded intensity fields. Consequently, the discriminator was trained to distinguish between real and generated thermal fields conditioned on the supplied process parameters, thereby learning the conditional distribution $p(Y \mid X)$, where X denoted the process–parameter image and Y represented the thermal profile.

The conditional character of the model therefore originated from the curated input representation and the paired data structure, rather than from an explicit conditioning term in the loss–function notation. During training, both real and generated thermal profiles were consistently evaluated by the discriminator in conjunction with the same conditioning image. As a result, the discriminator was compelled to assess whether the predicted thermal field was physically consistent with the supplied process parameters, rather than merely determining whether it resembled a plausible temperature distribution. A discriminator that ignored the conditioning image would have been unable to reliably differentiate real from generated samples, thereby enforcing effective utilization of the embedded process–parameter information during adversarial training.

It is further noted that this conditioning strategy differed fundamentally from conventional image–to–image translation tasks, in which input and output images typically exhibit pixel–wise spatial correspondence [46, 56, 57]. In the present work, the process–parameter images were deliberately constructed to lack spatial correlation with the target thermal fields. This design choice emphasized learning the underlying physical mapping between process parameters and thermal response, rather than relying on spatial alignment. Accordingly, the conditional Pix2Pix framework employed herein demonstrated that physically consistent thermal fields could be reconstructed from non–spatial process representations, highlighting the suitability of architecture–level conditionality for modeling thermo–kinetic evolution in laser powder bed fusion.

There was no universal rule for determining the values of λ_{L1}, and λ_{L2}. In the current work, these hyperparameters were fine-tuned through a process of trial-and-error.

L1 loss focuses on pixel-level accuracy by minimizing the absolute differences between the generated and target images, thus ensuring that each pixel matches closely with its counterpart. While beneficial for detailed fidelity, high L1 weights can sometimes lead to overly smoothed images where sharper details are needed. In contrast, L2 loss more stringently penalizes deviations between generated and target images, particularly targeting larger errors. This characteristic enables it to better preserve edge information and texture, making it more effective than L1 loss in maintaining temperature values within the thermal profile data.

In accordance with the theoretical assumptions, experimental observations on the SS316L dataset revealed distinct outcomes with three different combinations of L1, L2, and GAN weights. When L1 = L2 = 0 and GAN = 100, the high GAN weight resulted in images that were visually divergent from the target, as presented in the GAN model in Fig. 6. Increasing the L1 weight (i.e., L1 = 100, GAN = 1, and L2 = 0) produced images that were slightly improved compared to the GAN model, as observed in the L1 model in Fig. 6, However, this adjustment led to blurrier outputs due to the L1 loss's tendency to average pixel values. Conversely, increasing the L2 weight (i.e., L1 = 0, L2 = 100, and GAN = 1) yielded sharper and more accurate thermal maps, as illustrated by the L2 model in Fig. 6, proving particularly advantageous for this study. Consequently, the model was trained with an increased L2 weight (i.e., L1 = 0, L2 = 100, and GAN = 1) for all other materials.

4.2 Evolution of training

The ML model predictions of thermal profiles in four different materials across various epochs during training has been illustrated in Fig. 7 for the sake of comparison. The input process parameters were presented as source image, original out put from the FEM simulation was presented as the target image. The predicted images from the machine learning model at the initial, intermittent, and final epochs are displayed in Fig. 7. For SS316L dataset, optimal model performance was achieved at epoch 99 after approximately 17 hours of training, using a training dataset of 3,978 stitched images (training examples). For the AlSi10Mg dataset, optimal performance was reached at epoch 50 after about 11 hours of training, utilizing a dataset of 4,946 examples. The Cu dataset achieved its optimal model performance at epoch 199 after roughly 14 hours of training with 3,084 stitched images. Lastly, for the W dataset, the best performance was attained at epoch 47 after approximately 26 hours of training, with a dataset comprising 11,532 stitched images. All training sessions were conducted on a high-performance workstation featuring a 56-core/112-thread CPU, 256GB of RAM, and dual NVIDIA A6000 Quadro GPUs with a total of 96GB of dedicated GPU memory. Evaluation metrics, including MSE and SSIM, were employed to assess the model's performance. These metrics, reported along with their respective variabilities, provided insight into the model's accuracy and reliability in predicting the thermal profiles for all four materials.

All models employed the same training configuration across materials. Specifically, paired 256×256 source and target images were used with a batch size of 128. The Adam optimizer was applied to both generator and discriminator with learning rates of 1×10^{-4}. Loss weights were fixed as $\lambda_{L1} = 0$, $\lambda_{L2} = 100$, and $\lambda_{GAN} = 1$ for all materials, based on empirical evaluation of output fidelity and training stability.

5 Results and discussion

5.1 Model performance

This study examined the application of CGANs within the Pix2Pix framework to predict thermal profiles based on process parameters in the L-PBF-based additive manufacturing process. A defining aspect of this approach is the mapping of input process parameters, encoded as images, to thermal profiles, which represent spatial temperature distributions without any direct spatial correlation between the inputs and outputs. This contrasts with traditional image translation tasks, where input and output data typically share a spatial relationship. By leveraging an established image-to-image translation framework, this methodology not only demonstrated effective prediction capabilities under these conditions but also highlighted the potential to capitalize on rapid advancements in generative AI. Such an approach enables researchers and practitioners in materials science to deploy thermal profile prediction models with minimal programming expertise or modifications to the core network, thus lowering the barriers to adoption and extending its applicability in the field.

To assess the model's effectiveness, its performance was evaluated across both time-series and random time steps.

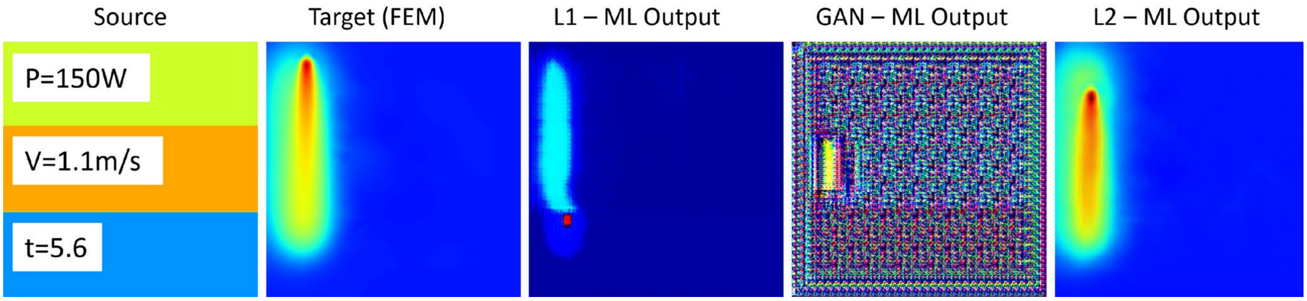

Fig. 6 Depiction of model performance based on L1, L2, and GAN loss functions, showing that the L2 loss function generates thermal profiles closely resembling the target thermal profile from FEM

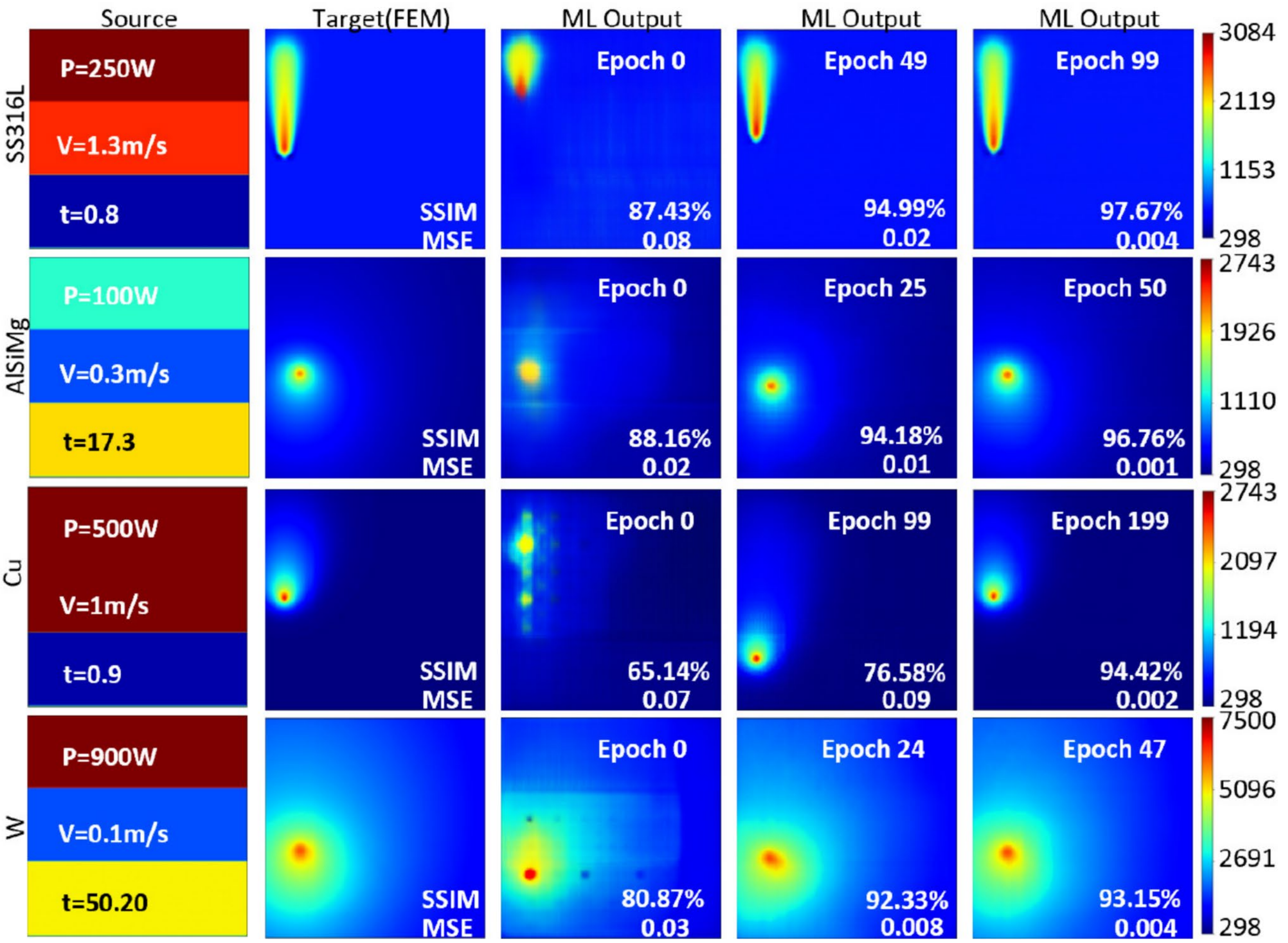

Fig. 7 Evolving inference capabilities of the model in predicting thermal profiles across initial, intermediate, and final epochs. Each row represents one of the following materials: SS316L, AlSi10Mg, Cu, and W. As training progresses, the predicted thermal profiles increasingly resemble the thermal profiles obtained through FEM

For the first case, input parameters power (P) and velocity (v) were fixed and time step (t) was varied. For the second case, different combinations of P and V were systematically varied, allowing for a comprehensive assessment of the model's performance. Figures 8 and 9 present visual and quantitative comparisons between target thermal profiles generated by FEM simulations and those predicted by the machine learning model, evaluated using SSIM, MSE, and maximum temperature of the thermal profiles. Figure 8 compares FEM simulated and machine learning model generated thermal profiles for time series test dataset of all four materials. As it can be observed, the model performed well on unseen test datasets across all four materials. The range of time steps [57-257] arises (Fig. 8) because the total number of time steps varies for each material depending on the power and velocity values. For example, some combinations of P and V take less time to complete the given (fixed in current case) scanning path, while others take longer.

The thermal profiles, shown in rows labeled as "Target (FEM)" and "Predicted (ML Output)" in Fig. 8(a) details the model's performance on SS316L test dataset for time series for $P = 150W$ and $V = 1.1m/s$. The comparison of machine learning predictions with FEM-generated thermal profiles demonstrated that the predictions were both visually and quantitatively similar to the FEM results. For instance, the maximum temperature $T(k)$ at $t = 57$ for FEM was $2890.93K$ and for ML output was $2845.51K$), indicating consistent accuracy across all time steps. This accuracy was observed for all four materials, with an average SSIM of 95.78% and an MSE of 0.0078 on the time series testing dataset.

Similarly, for AlSi10Mg (Fig. 8(b)) at $P = 150W$ and $V = 1.1m/s$, the average SSIM was 90.09% and MSE was 0.018. For Cu (Fig. 8(c)) at $P = 300W$ and $V = 0.5m/s$, the average SSIM was 89.29% and MSE was 0.027. For W (Fig. 8(d)), the average SSIM was 88.01% and MSE was 0.038. The ML predictions consistently captured the

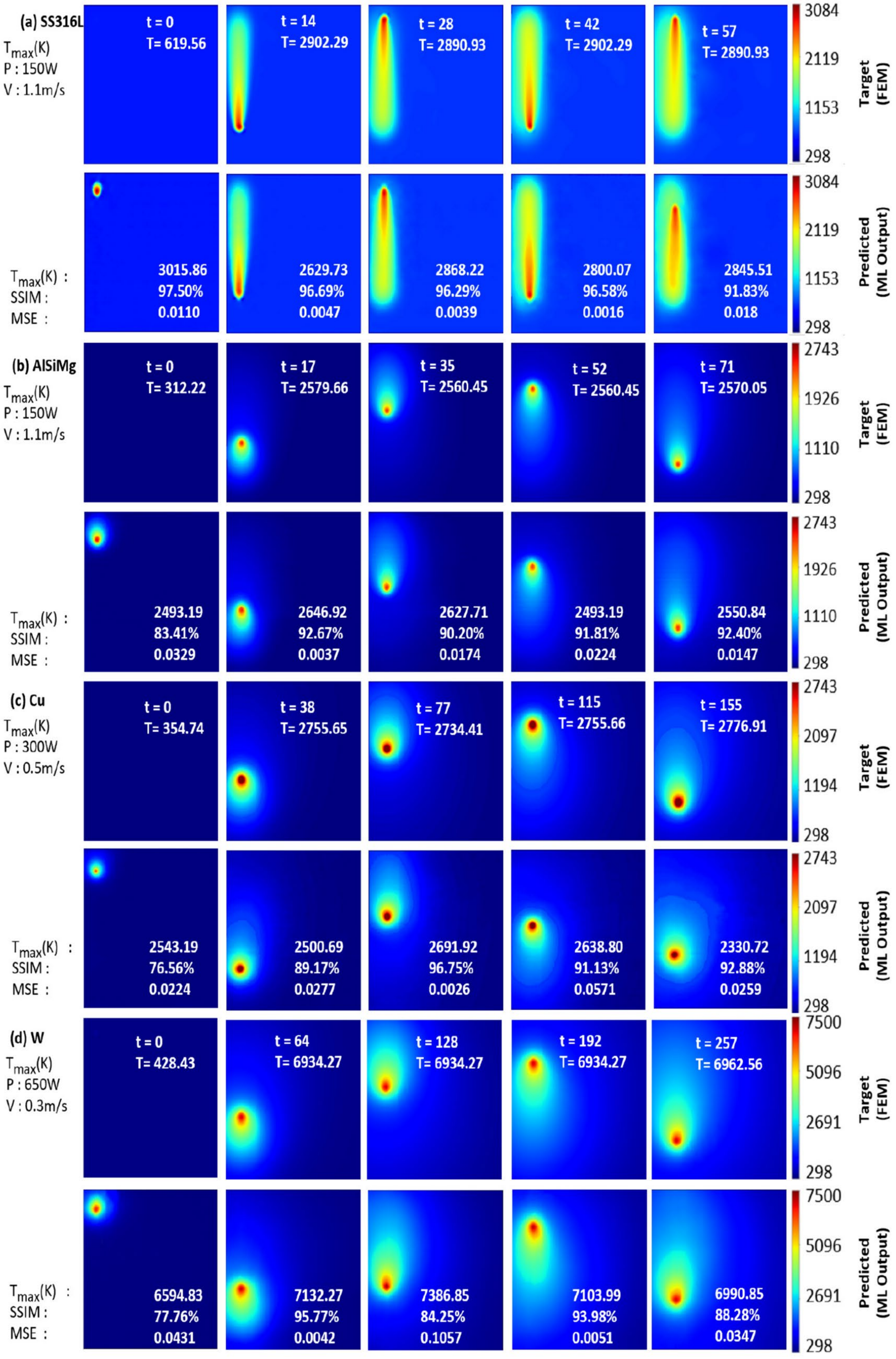

Fig. 8 Performance of the model visualized on time-series during the printing process for (**a**) SS316L, (**b**) AlSi10Mg, (**c**) Cu, and (**d**) W. The top row displays original thermal profiles from FEM simulations, while the bottom row presents ML-predicted thermal profiles for each material. Each pair of thermal profiles is accompanied by their corresponding MSE, SSIM, and maximum temperature ($T_{\max}$) values

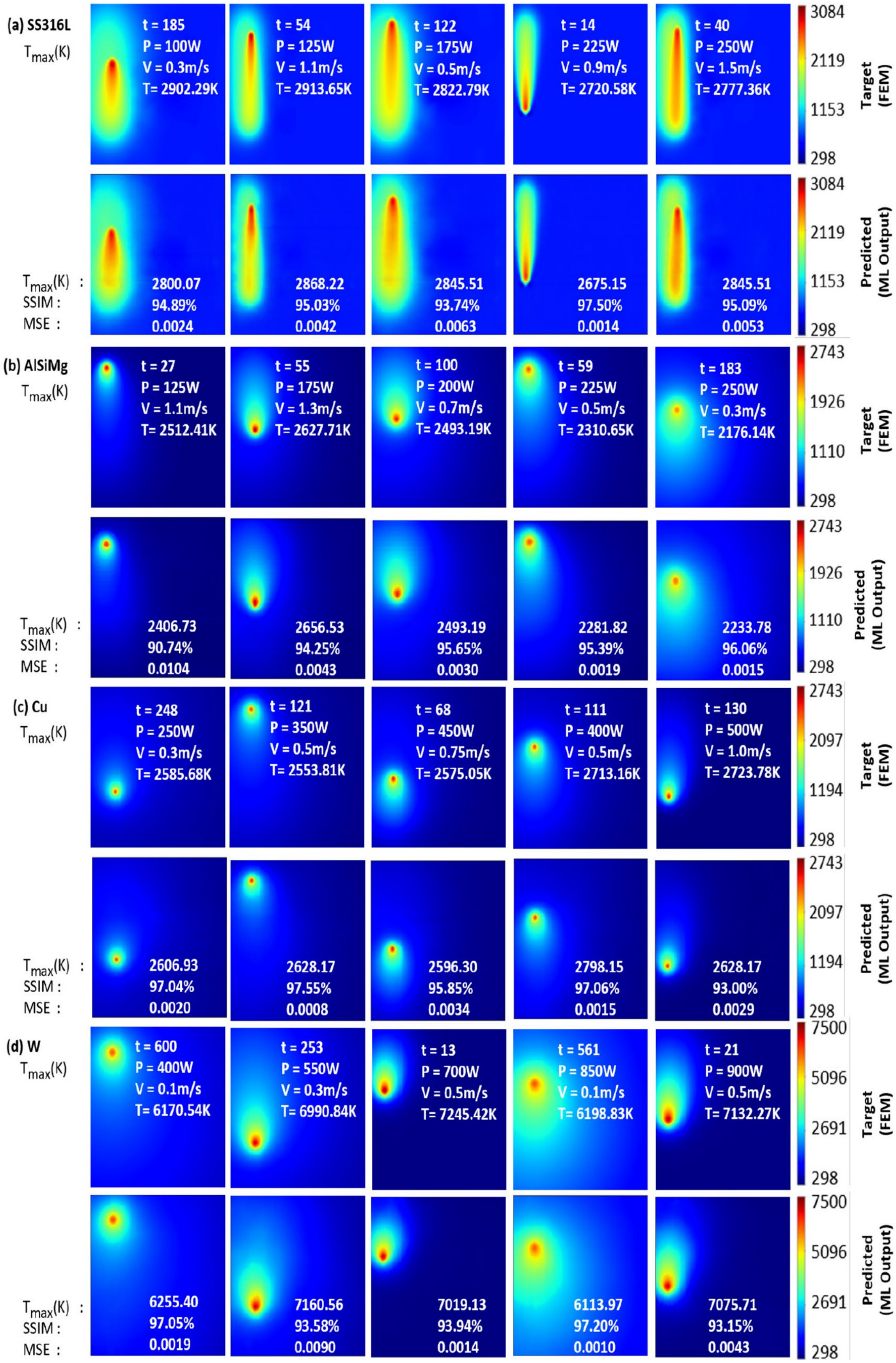

Fig. 9 Performance of the model on random testing dataset samples involving combinations of laser power, velocity, and time step for (**a**) SS316L, (**b**) AlSi10Mg, (**c**) Cu, and (**d**) W. The top row shows original thermal profiles from FEM, while the bottom row presents ML-predicted thermal profiles for each material alongside their corresponding MSE, SSIM, and maximum temperature ($T_{\max}$) values

temperature trends across all materials, with only the first time step showing the lowest SSIM and highest MSE values. This can be attributed to the fact that the model was trained on fewer examples of thermal profiles at time $t = 0$, as only 156 profiles were available for this initial state and this state is distinctly different from every other state (as laser is not present at $t = 0$).

The comparison of maximum temperatures between FEM and ML-generated thermal profiles did not always directly correlate with SSIM and MSE values, as these metrics evaluate pixel-wise differences between the images. Nonetheless, maximum temperature prediction remains a valuable metric for assessing the model's accuracy. Notably, in contrast to the pioneering study [12] that introduced upper cutoff temperatures to ensure network stability, the current approach did not require such cutoffs. The model successfully learned the targeted profiles without convergence issues, demonstrating the stability of the GAN-based network in handling sharp gradients typical of the AM process, which also resulted in faster convergence during the training phase.

Both visual and quantitative analyses, as demonstrated in Fig. 8 indicated that the machine learning model accurately captured the transient thermal evolution, maintaining high fidelity to the physical numerical values. For a more detailed visualization of the model's performance, time-series data is most effectively utilized. Readers are encouraged to refer to the video files (Videos I–IV) included in the online version of the manuscript for further insight.

For the second case, to enhance the model's robustness and reduce the risk of overfitting when using only time-series data. The model's performance at random time steps across SS316L, AlSi10Mg, Cu, and W materials, were evaluated for different combinations of input parameters (P, V, t). The FEM simulated thermal profiles from panels Fig. 9(a) to (d) of Fig. 9 delineated these parameter combinations alongside their respective maximum temperatures. Conversely, the machine learning model-generated thermal profiles provides detailed metrics such as SSIM, MSE, and maximum temperature values. For instance, in Fig. 9(a), at $t = 122$ for $P = 175W$ and $V = 0.5m/s$, the FEM simulated thermal profile recorded a maximum temperature of $2822.79K$. Meanwhile, the machine learning model predicted a maximum temperature of $2845.51K$ for the same conditions, with SSIM and MSE values of 93.74% and 0.0063, respectively. From the analysis of the model performance at random time steps, thermal profiles in Fig. 9 for different materials in panels Fig. 9(a) to (d), it was observed that the ML predicted thermal profiles closely aligned with the FEM simulated thermal profiles.

In addition to the maximum temperature ($T_{\max}$), the line thermal profiles along the x- and y-axes were extracted for quantitative evaluation. The extracted line thermal profiles also showed good agreement with the FEM thermal profiles for all four materials. Representatively, the temperature distribution as a function of distance for AlSi10Mg at $t = 92$ with $P = 100\,\mathrm{W}$ and $V = 0.5\,\mathrm{m/s}$, along both the x- and y-axes, is presented in Fig. 10. Over a distance of 2000 μm, the temperature ranged from approximately 290 K to 2000 K, with a MSE of 0.0089%. This representation was selected to demonstrate that the machine learning model accurately predicted numerical temperature values. Consequently, a model capable of predicting thermal profiles for different materials with comparable accuracy, as shown in Figs. 8 and 9, will facilitate efficient parameter optimization, quality control, and a comprehensive understanding of the AM process.

Performance of all the models considered in this present work for different materials are summarised in Table 6. It was

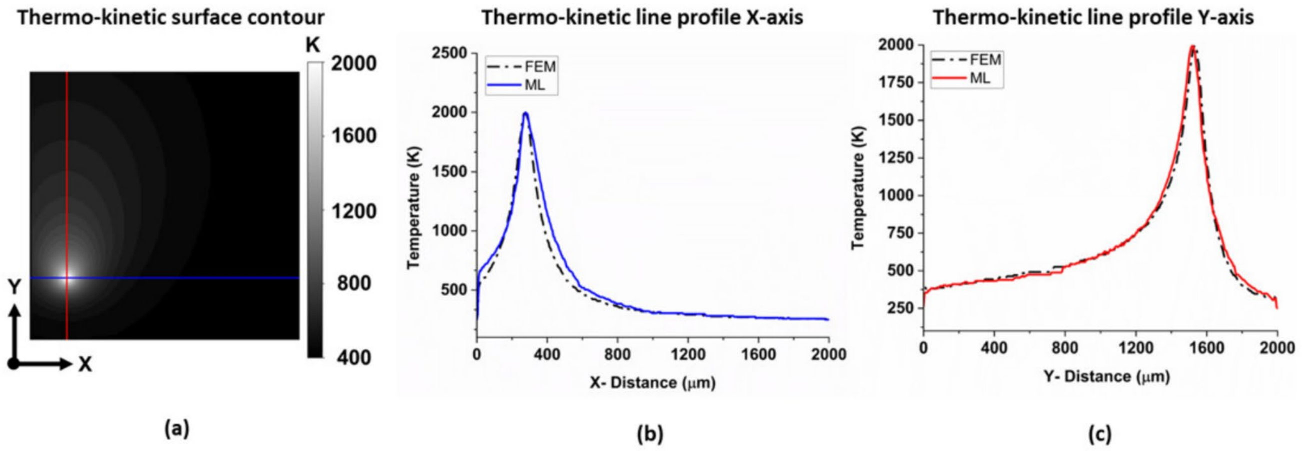

Fig. 10 (**a**) Representative thermal profiles for AlSi10Mg at 100W power and 0.5 m/s velocity (time step = 92) illustrating extraction of thermal data for spatial comparison. (**b**) spatial comparison of ML and FEM generated temperature profile along X-axis (along the "blue color" section represented in (**a**)) and (**c**) spatial comparison of ML and FEM generated temperature profile along Y-axis (along the "red color" section represented in (**a**))

Table 6 SSIM, MSE, and Maximum Thermal Gradient values across different range of parameter combinations of the model

Material	SSIM (%)	MSE	Maximum Thermal Gradient (K/m)
SS316L	95.49	0.006	2.18×10^7
AlSi10Mg	92.59	0.011	3.72×10^7
Cu	93.18	0.015	1.14×10^8
W	92.63	0.018	1.74×10^8

observed that the model exhibited reasonable performance with the SS316L dataset, surpassing the accuracy achieved with all other material datasets. This can be postulated to a comparatively lower thermal gradient of 2.18×10^7 K/m experienced by this material in comparison to other materials as presented in Table 6 during L-PBF AM processing.

In summary, the machine learning model generated thermal profiles that closely aligned with FEM-simulated thermal profiles, both visually and quantitatively, across time series and random time steps. Additionally, the line thermal profile temperature values were preserved, thus maintaining the physical integrity of the temperature distribution, as shown in Figs. 8, 9, and 10. The discriminator feedback enabled high SSIM, low MSE, and stable training despite large temperature gradients (2.18×10^7 to 1.74×10^8 K/m). The model successfully captured a broader temperature field over a $2000 \times 2000\ \mu\mathrm{m}^2$ area and accommodated diverse materials. While retraining is required for new parameters or materials, this approach establishes a foundation for generative thermal modeling in AM. Notably, this robustness is achieved using a standard Pix2Pix architecture with non-spatial process-parameter encodings, allowing architecture-agnostic extension to advanced Pix2Pix variants without modifying the core network design. Advancements in AI, particularly in generalization from limited datasets, could enhance scalability. Future research can refine these models for broader deployment.

6 Conclusion

In the present work, a conditional Pix2Pix architecture–based GAN framework was developed to predict thermal profiles in laser powder bed fusion using continuous variations of laser power, scan velocity, and time step, encoded as non–spatial, codified input images deliberately constructed without pixel–wise correspondence to the target thermal fields. The framework was trained on FEM–simulated datasets for SS316L, AlSi10Mg, Cu, and W, comprising 4,459, 5,544, 3,558, and 13,013 data files, respectively. Despite the absence of explicit spatial alignment between the inputs and outputs, the model successfully reconstructed sharp thermal gradients at the melt pool boundary, capturing the underlying physical relationship between process parameters and thermal response. High–fidelity thermal profiles were obtained for all four materials, yielding SSIM values of 95.49, 92.59, 93.18, and 92.63 and MSE values of 0.006, 0.011, 0.015, and 0.018, respectively, while maintaining physically consistent thermal behavior across a wide range of thermophysical properties.

The training data were generated using an FEM framework incorporating an experimentally calibrated volumetric heat source, with physical fidelity ensured through validation of melt pool dimensions and aspect ratios against in–house and literature measurements. The demonstrated robustness of the model across multiple materials highlights its potential extension to more complex scenarios, including multi–track and multi–layer builds with intricate scanning strategies. Inference was achieved at a rate of approximately 100 thermal profiles per second, enabling rapid exploration of large process–parameter spaces and significantly reducing computational cost relative to conventional numerical simulations. Nevertheless, the present framework did not explicitly account for melt pool convection, keyhole dynamics, or scan–history effects, and retraining was required for each material system. These limitations motivate future extensions based on transfer learning and more comprehensive multi–physics formulations, as well as the integration of physics–based constraints and experimental thermal data to further improve generalization in metal additive manufacturing.

Supplementary Information The online version contains supplementary material available at https://doi.org/10.1007/s00170-026-17732-3.

Acknowledgements Authors acknowledge the Center for Agile and Adaptive Additive Manufacturing (CAAAM) funded through State of Texas Appropriation: 190405-105-805008-220 for the infrastructure support, and Materials Research Facility (MRF) at the University of North Texas for the microscopy work.

Author Contributions The corresponding author (Narendra B Dahotre), on behalf of all the authors of this submission, declare that there are no financial and personal relationships with other people or organizations that could inappropriately influence this work. **Aishwarya Manjunath**: Writing – original draft, Methodology, Data processing, ML modeling, Conceptualization. **Venkata Mani Krishna Karri**: Writing – review & editing, Methodology, Validation, Formal analysis, ML modeling, Conceptualization. **Amrutha Anantatamukala**: Methodology, Validation, Formal analysis, ML modeling, Conceptualization. **Selvamurugan Palaniappan**: Writing – review & editing. **Shashank Sharma**: Writing – review & editing, Methodology, Validation, Formal analysis, FEM modeling, Conceptualization. **Song Fu**: Writing – review & editing, Supervision. **Narendra B Dahotre**: Writing – review & editing, Validation, Supervision, Project administration, Investigation, Formal analysis.

Funding Narendra B. Dahotre reports financial support was provided by State of Texas Appropriations: 190405-105-805008-220.

Data Availability Data will be made available on request.

Code Availability Code will be made available on request.

Materials Availability Not applicable.

Declarations

Competing interests The authors declare that they have no known competing financial interests or personal relationships that could have appeared to influence the work reported in this paper.

Ethics approval and consent to participate Not applicable.

Consent for publication Yes.

References

1. DebRoy T, Wei HL, Zuback JS, Mukherjee T, Elmer JW, Milewski JO, Beese AM, Wilson-Heid A, De A, Zhang W (2018) Additive manufacturing of metallic components-process, structure and properties. Prog Mater Sci 92:112–224. https://doi.org/10.1016/j.pmatsci.2017.10.001
2. Gordon JV, Narra SP, Cunningham RW, Liu H, Chen H, Suter RM, Beuth JL, Rollett AD (2020) Defect structure process maps for laser powder bed fusion additive manufacturing. Addit Manuf 36:101552. https://doi.org/10.1016/j.addma.2020.101552
3. Ness KL, Paul A, Sun L, Zhang Z (2022) Towards a generic physics-based machine learning model for geometry invariant thermal history prediction in additive manufacturing. J Mater Process Technol 302:117472. https://doi.org/10.1016/j.jmatprotec.2021.117472
4. Ho S, Zhang W, Young W, Buchholz M, Al Jufout S, Dajani K, Bian L, Mozumdar M (2021) Dlam: Deep learning based real-time porosity prediction for additive manufacturing using thermal images of the melt pool. IEEE Access 9:115100–115114. https://doi.org/10.1109/ACCESS.2021.3105362
5. Zhan J, Li Y, Guo Z, Ma R, Wang S, Yang X, Jarlöv A, Cao H, Lin F, Xu Y, Li K, Zhang Y-W, Zhou K (2026) A 4d-printed niti alloy with encoded microstructures evades the cooling capacity-energy efficiency trade-off in elastocaloric refrigeration. Mater Sci Eng R Rep 169:101191. https://doi.org/10.1016/j.mser.2026.101191
6. Zhan J, Li K, Ma R, Zhu L, Fang J, Cao H, Zhang DZ, Murr LE (2024) Achieving fine tailoring of elastocaloric properties of laser powder bed-fused niti alloy via laser beam manipulation. Int J Mach Tools Manuf 202:104210. https://doi.org/10.1016/j.ijmachtools.2024.104210
7. Li K, Fang J, Zhan J, Ma R, Wang S, Yang X, Zhang DZ, Murr LE, Cao H (2025) Elastocaloric effect of laser powder bed fused niti alloy with customizable hierarchical heterogeneous microstructure. Addit Manuf 97:104619
8. Xiong Z, Li H, Yang H, Yang Y, Liu Y, Cui L, Li X, Masseling L, Shen L, Hao S (2022) Micro laser powder bed fusion of niti alloys with superior mechanical property and shape recovery function. Addit Manuf 57:102960
9. Xie J, Chai Z, Xu L, Ren X, Liu S, Chen X (2022) 3d temperature field prediction in direct energy deposition of metals using physics informed neural network. The International Journal of Advanced Manufacturing Technology 119(5):3449–3468. https://doi.org/10.1007/s00170-021-08542-w
10. Palaniappan, S., Krishna, K.M., Radhakrishnan, M., Sharma, S., Ramalingam, M.S., Banerjee, R., Dahotre, N.B.:Thermokinetics driven microstructure and phase evolution in laser-based additive manufacturing of Ti-25wt.% Nband its performance in physiological solution. Materialia, 102190 (2024) https://doi.org/10.1016/j.mtla.2024.102190
11. Zhou Z, Shen H, Liu B, Du W, Jin J (2021) Thermal field prediction for welding paths in multi-layer gas metal arc welding-based additive manufacturing: A machine learning approach. J Manuf Process 64:960–971. https://doi.org/10.1016/j.jmapro.2021.02.033
12. Hemmasian A, Ogoke F, Akbari P, Malen J, Beuth J, Farimani AB (2023) Surrogate modeling of melt pool temperature field using deep learning. Additive Manufacturing Letters 5:100123. https://doi.org/10.1016/j.addlet.2023.100123
13. Guo S, Agarwal M, Cooper C, Tian Q, Gao RX, Grace WG, Guo Y (2022) Machine learning for metal additive manufacturing: Towards a physics-informed data-driven paradigm. J Manuf Syst 62:145–163. https://doi.org/10.1016/j.jmsy.2021.11.003
14. Ren K, Chew Y, Zhang Y, Fuh J, Bi G (2020) Thermal field prediction for laser scanning paths in laser aided additive manufacturing by physics-based machine learning. Comput Methods Appl Mech Eng 362:112734. https://doi.org/10.1016/j.cma.2019.112734
15. Anantatamukala A, Krishna KM, Dahotre NB (2023) Generative adversarial networks assisted machine learning based automated quantification of grain size from scanning electron microscope back scatter images. Mater Charact 206:113396. https://doi.org/10.1016/j.matchar.2023.113396
16. S K, Durgadevi M (2021) Generative adversarial network (gan): a general review on different variants of gan and applications. In: 2021 6th International Conference on Communication and Electronics Systems (ICCES), pp 1–8. https://doi.org/10.1109/ICCES51350.2021.9489160
17. Cao Z, Liu Q, Liu Q, Yu X, Kruzic JJ, Li X (2023) A machine learning method to quantitatively predict alpha phase morphology in additively manufactured ti-6al-4v. npj Computational Materials 9(1):195. https://doi.org/10.1038/s41524-023-01152-y
18. Hsu T, Epting WK, Kim H, Abernathy HW, Hackett GA, Rollett AD, Salvador PA, Holm EA (2021) Microstructure generation via generative adversarial network for heterogeneous, topologically complex 3d materials. JOM 73:90–102. https://doi.org/10.1007/s11837-020-04484-y
19. Senapati RK, Satvika R, Anmandla A, Ashesh Reddy G, Anil Kumar C (2023) Image-to-image translation using pix2pix gan and cycle gan. In: International Conference on Data Intelligence and Cognitive Informatics, pp 573–586. https://doi.org/10.1007/978-981-99-7962-2_42 Springer
20. Ouidadi H, Guo S (2024) Mps-gan: A multi-conditional generative adversarial network for simulating input parameters' impact on manufacturing processes. J Manuf Process 131:1030–1045. https://doi.org/10.1016/j.jmapro.2024.09.067
21. Guo S, Guo W, Bian L, Guo YB (2023) A deep-learning-based surrogate model for thermal signature prediction in laser metal deposition. IEEE Trans Autom Sci Eng 20(1):482–494. https://doi.org/10.1109/TASE.2022.3158204
22. Bourou A, Mezger V, Genovesio A (2024) Gans conditioning methods: A survey. arXiv preprint arXiv:2408.15640
23. Xu S, Rai R, Moore RD, Orlandi G, Abdeljawad F (2024) Mptp-net: melt pool temperature profile network for thermal field modeling in beam shaping of laser powder bed fusion. J Intell Manuf, pp 1–17. https://doi.org/10.1007/s10845-024-02449-5
24. Dahotre NB, Pantawane MV, Sharma S (eds) (2022) Laser-based Additive Manufacturing: Modeling, Simulation, and Experiments. Wiley-VCH GmbH, Weinheim, Germany. https://doi.org/10.1002/9783527828814
25. Sharma S, Joshi SS, Pantawane MV, Radhakrishnan M, Mazumder S, Dahotre NB (2023) Multiphysics multi-scale computational framework for linking process-structure-property relationships in metal additive manufacturing: A critical review. Int Mater Rev

68(12):943–1009. https://doi.org/10.1080/09506608.2023.2169501

26. Patel S, Vlasea M (2020) Melting modes in laser powder bed fusion. Materialia 9:100591. https://doi.org/10.1016/j.mtla.2020.100591
27. Parsazadeh M, Sharma S, Dahotre N (2023) Towards the next generation of machine learning models in additive manufacturing: A review of process dependent material evolution. Prog Mater Sci. https://doi.org/10.1016/j.pmatsci.2023.101102
28. Moges T, Ameta G, Witherell P (2019) A review of model inaccuracy and parameter uncertainty in laser powder bed fusion models and simulations. J Manuf Sci E T ASME 141. https://doi.org/10.1115/1.4042789/475003
29. Ross AJ, Bitharas I, Perkins KG, Moore AJ (2022) Volumetric heat source calibration for laser powder bed fusion. Addit Manuf 60:103267. https://doi.org/10.1016/j.addma.2022.103267
30. Mukherjee T, Wei HL, De A, DebRoy T (2018) Heat and fluid flow in additive manufacturing - part ii: Powder bed fusion of stainless steel, and titanium, nickel and aluminum base alloys. Comput Mater Sci 150:369–380. https://doi.org/10.1016/j.commatsci.2018.04.027
31. Pantawane MV, Sharma S, Sharma A, Dasari S, Banerjee S, Banerjee R, Dahotre NB (2021) Coarsening of martensite with multiple generations of twins in laser additively manufactured ti6al4v. Acta Mater 213. https://doi.org/10.1016/j.actamat.2021.116954
32. Zagade P, Gautham BP, De A, DebRoy T (2021) Analytical estimation of fusion zone dimensions and cooling rates in part scale laser powder bed fusion. Addit Manuf 46:102222. https://doi.org/10.1016/j.addma.2021.102222
33. Weaver JS, Heigel JC, Lane BM (2022) Laser spot size and scaling laws for laser beam additive manufacturing. J Manuf Process 73:26–39. https://doi.org/10.1016/j.jmapro.2021.10.053
34. Ye J, Khairallah SA, Rubenchik AM, Crumb MF, Guss G, Belak J, Matthews MJ (2019) Energy coupling mechanisms and scaling behavior associated with laser powder bed fusion additive manufacturing. Adv Eng Mater 21(1):1900185. https://doi.org/10.1002/adem.201900185
35. Rubenchik AM, King WE, Wu SS (2018) Scaling laws for the additive manufacturing. J Mater Process Technol 257:234–243. https://doi.org/10.1016/j.jmatprotec.2018.02.034
36. Fabbro R (2019) Scaling laws for the laser welding process in keyhole mode. J Mater Process Technol 264:346–351. https://doi.org/10.1016/j.jmatprotec.2018.09.027
37. Sharma S, Krishna KVM, Joshi SS, Radhakrishnan M, Palaniappan S, Dussa S, Banerjee R, Dahotre NB (2023) Laser based additive manufacturing of tungsten: Multi-scale thermo-kinetic and thermo-mechanical computational model and experiments. Acta Mater 259. https://doi.org/10.1016/j.actamat.2023.119244
38. Zhang J, Gu D, Yang Y, Zhang H, Chen H, Dai D, Lin K (2019) Influence of particle size on laser absorption and scanning track formation mechanisms of pure tungsten powder during selective laser melting. Engineering 5:736–745. https://doi.org/10.1016/j.eng.2019.07.003
39. Jadhav SD, Goossens LR, Kinds Y, Hooreweder BV, Vanmeensel K (2021) Laser-based powder bed fusion additive manufacturing of pure copper. Addit Manuf 42:101990. https://doi.org/10.1016/j.addma.2021.101990
40. Haynes WM (2015) Handbook of Chemistry and Physics, 95th edn. CRC, New York
41. Tang C, Le KQ, Wong CH (2020) Physics of humping formation in laser powder bed fusion. Int J Heat Mass Transf 149:119172. https://doi.org/10.1016/j.ijheatmasstransfer.2019.119172
42. Cagran C (2000) Thermal conductivity and thermal diffusivity of liquid copper. Technical report, Technische Universitat Graz
43. Assael MJ, Kalyva AE, Antoniadis KD, Banish RM, Egry I, Wu J, Kaschnitz E, Wakeham WA (2010) Reference data for the density and viscosity of liquid copper and liquid tin. J Phys Chem Ref Data 39:33105. https://doi.org/10.1063/1.3467496
44. Dai D, Gu D (2015) Tailoring surface quality through mass and momentum transfer modeling using a volume of fluid method in selective laser melting of tic/alsi10mg powder. Int J Mach Tools Manuf 88:95–107. https://doi.org/10.1016/j.ijmachtools.2014.09.010
45. Aboulkhair NT, Maskery I, Tuck C, Ashcroft I, Everitt NM (2016) On the formation of alsi10mg single tracks and layers in selective laser melting: Microstructure and nano-mechanical properties. J Mater Process Technol 230:88–98
46. Isola P, Zhu J-Y, Zhou T, Efros AA (2017) Image-to-image translation with conditional adversarial networks, pp 5967–5976. https://doi.org/10.1109/CVPR.2017.632
47. Isola P, Zhu J-Y, Zhou T, Efros AA (2017) Image-to-image translation with conditional adversarial networks. In: Proceedings of the IEEE conference on computer vision and pattern recognition, pp 1125–1134. https://doi.org/10.48550/arXiv.1611.07004
48. Xun S, Li D, Zhu H, Chen M, Wang J, Li J, Chen M, Wu B, Zhang H, Chai X et al (2022) Generative adversarial networks in medical image segmentation: A review. Comput Biol Med 140:105063. https://doi.org/10.1016/j.compbiomed.2021.105063
49. Liu K, Ye Z, Guo H, Cao D, Chen L, Wang F-Y (2021) Fiss gan: A generative adversarial network for foggy image semantic segmentation. IEEE/CAA Journal of Automatica Sinica 8(8):1428–1439. https://doi.org/10.1109/JAS.2021.1004057
50. Yi X, Walia E, Babyn P (2019) Generative adversarial network in medical imaging: A review. Med Image Anal 58:101552. https://doi.org/10.1016/j.media.2019.101552
51. Setiowati S, Franita EL, Ardiyanto I et al (2017) A review of optimization method in face recognition: Comparison deep learning and non-deep learning methods. In: 2017 9th International Conference on Information Technology and Electrical Engineering (ICITEE), pp 1–6. IEEE
52. Kingma DP, Ba J (2014) Adam: A method for stochastic optimization. arXiv preprint arXiv:1412.6980
53. Bischl B, Binder M, Lang M, Pielok T, Richter J, Coors S, Thomas J, Ullmann T, Becker M, Boulesteix A-L et al (2023) Hyperparameter optimization: Foundations, algorithms, best practices, and open challenges. Wiley Interdisciplinary Reviews Data Mining and Knowledge Discovery 13(2):1484
54. Minaee S, Boykov Y, Porikli F, Plaza A, Kehtarnavaz N, Terzopoulos D (2021) Image segmentation using deep learning: A survey. IEEE Trans Pattern Anal Mach Intell 44(7):3523–3542
55. Wang Z, Bovik AC, Sheikh HR, Simoncelli EP (2004) Image quality assessment: from error visibility to structural similarity. IEEE Trans Image Process 13(4):600–612
56. Goodfellow I, Pouget-Abadie J, Mirza M, Xu B, Warde-Farley D, Ozair S, Courville A, Bengio Y (2014) Generative adversarial nets. Advances in neural information processing systems 27. https://doi.org/10.48550/arXiv.1406.2661
57. Mirza M, Osindero S (2014) Conditional generative adversarial nets. arXiv preprint arXiv:1411.1784, https://doi.org/10.48550/arXiv.1411.1784